Additive Manufacturing 41 (2021) 101993

Contents lists available at ScienceDirect

Additive Manufacturing

journal homepage: www.elsevier.com/locate/addma

Porosity in wire arc additive manufacturing of aluminium alloys

Tobias Hauser [a,d,*], Raven T. Reisch [b,d], Philipp P. Breese [c,d], Benjamin S. Lutz [d], Matteo Pantano [d], Yogesh Nalam [d], Katharina Bela [d], Tobias Kamps [d], Joerg Volpp [a], Alexander F. H. Kaplan [a]

[a] Department of Engineering Sciences and Mathematics, Luleå University of Technology, S-971 87 Luleå, Sweden
[b] Chair of Robotics, Artificial Intelligence and Real-time Systems, Technical University of Munich, D-80333 Munich, Germany
[c] Coating Technology, Technical University Berlin, Pascalstr. 8–9, D-10587 Berlin, Germany
[d] Technology department, Siemens AG, D-81739 Munich, Germany

ARTICLE INFO

Keywords:
WAAM
Robot-based
Anomaly
Monitoring
Computer vision

ABSTRACT

Wire Arc Additive Manufacturing is a near-net-shape processing technology which allows cost-effective manufacturing of large and customized metal parts. Processing of aluminium in Wire Arc Additive Manufacturing is quite challenging, especially in terms of porosity. In the present work, pore behaviour in Wire Arc Additive Manufacturing of AW4043/AlSi5(wt%) was investigated and a post-process monitoring approach was developed. It has been observed that as the shielding gas flow rate increases, the porosity in aluminium parts also increases due to the rapid solidification of the melt pool by forced convection. The higher convection rate seems to limit the escape of gas inclusions. Furthermore, gas inclusions escaping from the melt pool leave cavities on the surface of each deposited layer. Process camera imaging is used to monitor these cavities to acquire information about the porosity in the part. The observations were supported by Computational Fluid Dynamics simulations which show that the gas flow rate correlates with the porosity in aluminium parts manufactured by Wire Arc Additive Manufacturing. Since a lower gas flow rate leads to reduced convective cooling, the melt pool remains liquid for a longer period allowing pores to escape for a longer period and thus reducing porosity. Based on these investigations, a monitoring approach is presented.

1. Introduction

1.1. Wire Arc Additive Manufacturing

Wire Arc Additive Manufacturing (WAAM) is a near-net-shape processing technology that is classified as one of the Direct Energy Deposition (DED) processes [1,2]. The process is primarily intended for cost-effective production of large components due to its high deposition rates compared to other Additive Manufacturing technologies e.g. laser-based Additive Manufacturing processes [3]. The wire-based techniques are 2–50 times more cost efficient than powder-based techniques [1,2]. Currently, most WAAM processes are based on Gas Metal Arc Welding (GMAW), which has a high energy input into the base material due to the temperatures of the arc reaching up to 10 000 K [4]. Since the energy input is so high, a constant temperature range is of high importance for WAAM, as Hauser et al. have already proved by detecting geometric deviations in the part due to excessively high process temperatures [5]. One of the most promising GMAW avenues for a future industrial use of WAAM is the Cold Metal Transfer (CMT) process which enables a reduced energy input compared to other GMAW processes [6–8]. In the CMT process, the wire is conveyed into the process zone with a pushing and pulling movement [7,9,10]. In one CMT cycle, a pulse of defined duration melts the wire tip, which is fed forward until it touches the melt pool, produces a short-circuit and arc extinction [7]. Afterwards the wire is mechanically pulled back, separating the wire from the melt pool [7]. Then the CMT cycle restarts.

1.2. Aluminium alloys in WAAM

WAAM has been recognized as one of the most efficient processing

* Correspondence to: Luleå Tekniska Universitet, 971 87 Luleå, Sweden.
E-mail addresses: tobias.hauser@ltu.se (T. Hauser), raven.reisch@tum.de (R.T. Reisch), philipp.breese@siemens.com (P.P. Breese), lutz.benjamin@siemens.com (B.S. Lutz), matteo.pantano@siemens.com (M. Pantano), yogesh.nalam.ext@siemens.com (Y. Nalam), katharina.bela@siemens.com (K. Bela), tobias.kamps@siemens.com (T. Kamps), jorg.volpp@ltu.se (J. Volpp), Alexander.Kaplan@ltu.se (A.F.H. Kaplan).

https://doi.org/10.1016/j.addma.2021.101993
Received 2 December 2020; Received in revised form 24 February 2021; Accepted 29 March 2021
Available online 6 April 2021

methods for cost-effective production of large structural parts [11–13]. However, the process is not widely used for aluminium alloys due to a lack of process understanding. Aluminium alloys are widely used in different industrial fields such as aerospace, ship building, train building, and automotive industries because of their light weight and high corrosion resistance [13,14]. Besides ultra-pure aluminium (Al), various aluminium alloys are used. The most important alloying elements are copper, silicon, magnesium, zinc, and manganese [15,16]. Aluminium alloys of the EN AW-4000 series are common for welding applications, which makes them a promising alloy for Additive Manufacturing. Silicon (Si) is the main alloy component in the 4000 Al-alloy series. Köhler et al. performed WAAM for AlSi12(wt%) and studied process characteristics, mechanical properties, and residual stresses [17]. They suggested that a wide solidification range (temperature range between solidus and liquidus temperature) of the alloy is likely to lead to a smooth track [17]. Furthermore, they found that the material properties are evenly distributed over the manufactured geometry when the interpass temperature (temperature of the part before a new layer is deposited) is kept constant [17]. The big challenges in WAAM of aluminium are the occurrence of anomalies such as cracks, surface oxidation, and porosity.

1.3. Porosity in WAAM of aluminium alloys

Porosity reduces the overall density of the parts and thus reduces the mechanical properties (such as the tensile strength) of the manufactured components [18]. Porosity is a general problem when processing most aluminium alloys and should be avoided or kept as low as possible in order to alter the mechanical properties as little as possible [18]. Pores can be mainly classified into the small and homogenously distributed hydrogen pores, with a diameter up to 100 μm, and into the big and inhomogeneously distributed process pores [19]. Hydrogen pores are distributed more homogenously than process related pores [18]. Hydrogen is one of the main drivers in pore formation during WAAM of aluminium because of the difference in the solubility of hydrogen in aluminium liquid (at 0.69 cm^3 per 100 g) and solid (at 0.036 cm^3 per 100 g) [19–21]. One of the major hydrogen sources is the wire with moisture, grease, and hydrocarbon contaminants on its surface which can vaporize in the arc and convert into atomic hydrogen [19]. Process related pores are distributed more inhomogeneously and can be caused by entrapment of shielding gas, air (oxygen and nitrogen), or other gases which cannot escape due to the rapid solidification of aluminium [18]. Aluminium has a very low melting point and a very high thermal conductivity compared to other materials e.g. steel, so the solidification rate is relatively high and gas bubbles cannot easily escape. Argon and helium are the main gases used as shielding gas for aluminium welding [18]. Helium is much more expensive than argon and the gas flow rate of helium must be about three times higher than argon due to the lower density of helium [18]. Argon is therefore more commonly used in industrial manufacturing [22]. However, pure helium is not used as shielding gas, but argon-helium mixtures are used, which produce a lower amount of gas bubbles as weld porosity sources due to a more stable arc by the helium content [23]. Furthermore, for welding with argon-helium mixtures, the arc energy is higher as with pure argon gas, resulting in a higher heat input into the process [18,23]. Compared to conventional gas supply methods, the addition of helium in aluminium welding therefore leads to a lower porosity and a deeper weld profile [22].

Gu et al. showed for the aluminium alloys AlCu6MnZrTi and AlMg4,5MnZr that, after heat treatment, Ostwald ripening and hydrogen diffusion dominate pore growth [19]. Ostwald ripening causes merging of small pores into larger ones [19]. In conclusion, the porosity can be even higher after heat treatment [19]. Gu et al. also showed that porosity can be reduced through inter-layer cold working [19]. Wang et al. investigated the impact of arc current and arc pulse frequency on the porosity and grain structure of WAAM based on Gas Tungsten Arc Welding and found that with increasing pulse frequency, the grains became coarser and the porosity initially decreased and reached its minimum at 50 Hz due to the decreased liquid viscosity, which lead to an increased escape rate for pores [24]. However, porosity increased again for frequencies higher than 50 Hz due to the relationship between pore formation and nucleation caused by the higher pulse frequencies [24]. Derekar et al. investigated the influence of the interpass temperature on the porosity of aluminium parts manufactured by WAAM and observed that a higher interpass temperature reduces porosity [20]. Cong et al. performed experiments for WAAM of Al-6.3%Cu with different CMT modes and found that the porosity can be significantly reduced by the CMT-Pulse Advanced mode [25]. In general, several scientific studies have shown that the porosity decreases if the melt pool remains in the molten state as long as possible, so that gas inclusions have enough time to escape.

Generally, the porosity is examined after the component is manufactured, but there are also approaches which detect anomalies during the process. Various research groups are working on non-destructive monitoring systems for anomalies such as porosity to improve the process reliability in WAAM [26–30]. Lopez et al. investigated different non-destructive testing methods and demonstrated that existing techniques such as radiography and ultrasound can be used for in-process and off-line inspection of WAAM parts regarding defects such as pores and cracks [29]. Bento et al. showed that it is possible to detect defects during WAAM of aluminium by eddy current testing [27]. The disadvantage of this method is its rather complex set-up, which takes a lot of time and increases the processing time [27]. Javadi et al. also showed that ultrasonic phased arrays can be used to detect big pores and cracks during WAAM by detecting changes in the ultrasonic signal [26]. However, detection of small pores was not possible with this method [26]. Zhang et al. used process imaging in combination with convolutional neural network models to monitor porosity during laser additive manufacturing [31]. Since all monitoring approaches have their advantages and disadvantages, Reisch et al. presented a context-sensitive, multivariate in-process monitoring system with different sensors to increase the probability that an anomaly is detected [32].

WAAM of aluminium has great potential to be widely used in industry, but further research still needs to be done to increase the understanding of the process and to ensure high quality parts are produced. In the present work, pore behaviour in Wire Arc Additive Manufacturing of AW4043/AlSi5(wt%) was investigated and a post-process monitoring approach was developed. The reduction of porosity in WAAM of aluminium is a critical topic for a long time which was investigated by different researchers. Several methods were developed to suppress the formation of porosity but just a few methods for monitoring of porosity in parts were introduced. In this work, process camera imaging and Computer Vision methods were used to monitor the porosity within parts. The findings were supported by microstructural analysis and Computational Fluid Dynamics simulations.

2. Material and methods

2.1. Aluminium alloys

For investigation of the gas flow rate influence in WAAM, walls with different gas flow rates from 6 to 10 litres per minute (l/min) were manufactured. The experiments were carried out with AlSi5 (wt%) wire with a wire diameter of 1.2 mm. Substrate plates of AlMg1SiCu (wt%) with the dimensions 120 mm × 100 mm x 5 mm were used. The chemical compositions of the two alloys are shown in Table 1.

2.2. Experimental set-up

In the robot-based WAAM set-up shown in Fig. 1, a 6-axis Comau robot, a Comau tilting turn table, a Siemens motion control, and a Fronius welding source with CMT functionality were used. For in-process monitoring, a Cavitar welding camera C200 was employed.

Table 1
Chemical composition of the aluminium alloys used, in wt% [33].

Alloy	Al	Si	Fe	Cu	Mn	Mg	Zn	Cr	Ti
AlSi5	Bal.	4.5–6	0.8	0.3	0.05	0.05	0.1	–	0.2
AlMg1SiCu	Bal.	0.4–0.8	0.7	0.15–0.4	0.15	0.8–1.2	0.25	0.04–0.35	0.15

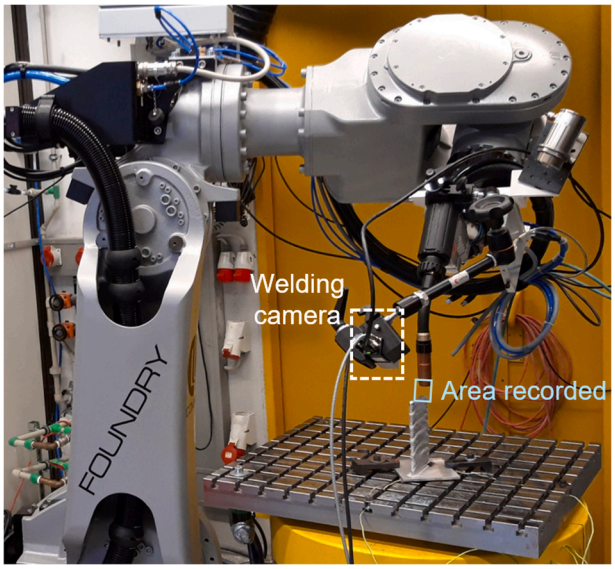

Fig. 1. Set-up of the robot-based WAAM-system with in-process monitoring by a welding camera (marked white) with the area recorded (marked blue).

All experiments were conducted with a vertical orientation of the torch, through which the wire is fed perpendicular to the substrate as shown in Fig. 2. In the experiments, a wall was built by processing ten layers on top of each other with a layer height of 1.5–2.0 mm. The first two layers were created with the CMT+P (Pulsed cold metal transfer) mode because the energy input in that mode is higher than in the CMT mode and therefore a better bonding of the wall with the substrate is created. After the first two layers, the process was switched to CMT mode. In order to create a smooth wall, the interpass temperature was kept in a temperature range due to a changing wire feed speed, which was reduced from 5 m/min in the first layer to 4 m/min in the second layer and to a constant 3 m/min starting from the third layer. The build-up was based on a zigzag strategy in which material was deposited in one direction only and then the robot moved back, resulting in a cooling time of five seconds between layers. In the CMT process, each layer consists of an ignition phase, a process phase, and a shutdown phase. In the ignition phase, the energy input is higher to initiate the arc-based process. In the process phase the set parameters are used, and in the shutdown phase the robot stops its movement but continues the deposition to fill the end zone using a lower power level. The parameters used for the experiments are listed in Table 2. The shielding gas was fed through the torch with an orifice diameter of 18 mm. The parameter varied in these experiments was the shielding gas flow rate, which was manually controlled by a flow meter from 6 l/min to 10 l/min. For lower gas flow rates as 6 l/min, main oxidation effects were observed and therefore lower gas flow rates were not investigated.

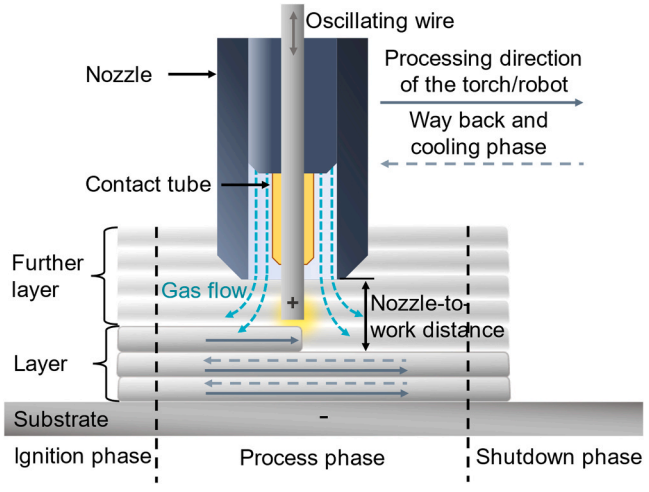

Fig. 2. Schematic torch set-up for Wire Arc Additive Manufacturing.

2.3. Welding camera

To monitor and analyse the melt pool during WAAM a C200 (Cavitar) process camera was used. The process was monitored from the front at an angle of 30° to the horizontal with a frame rate of 30 frames per second. The resolution of the welding camera was 1980 pixels x 1080 pixels and the actual size per pixel was 73.5 µm. The camera has an integrated laser unit with a wavelength of 640 nm which is used as an illumination laser. For very bright processes such as WAAM, the laser unit is used to illuminate the process at a specific wavelength, while all other process-related radiations outside the wavelength of 640 nm are filtered to obtain a non-saturated view on the melt pool. The process images were captured during processing and during the cooling phase as the robot moved back to the start position of the next layer. Correlations between pore formation and process images, capturing the melt pool behaviour and the solidified layer, were investigated. A monitoring solution based on the results of the investigations was developed in the programming language Python. The Python libraries OpenCV, argparse, matplotlib, and numpy were used. As a first step the process videos were inverted to increase the visibility of the cavities, as shown in Fig. 3. Subsequently an appropriate threshold was set for the background subtraction method which was used to filter cavities from the process images. The threshold in this Background Subtraction Method is a brightness limit which ensures that pixels with a brightness below this limit are displayed black and pixels with a brightness above this limit are displayed white. The cavities (white pixels) in the region of interest (marked blue) were captured over time and visualized in the diagrams,

Table 2
Process parameters used for WAAM of AlSi5(wt%).

Parameter	Value
Wire material	AlSi5(wt%)
Wire diameter	1.2 mm
Substrate material	AlSi1MgMn(wt%)
Ignition phase length	10 mm
Process phase length	60 mm
Shutdown phase length	10 mm
Wire feed speed	3–5 m/min
Current – CMT+P mode	113 A
Voltage – CMT+P mode	17.4 V
Current - CMT mode	50 A
Voltage - CMT mode	11.2 V
Robot travel speed	0.35 m/min
Shielding gas	Argon 4.5 (99.995% purity)
Gas flow rate	6–10 l/min
Nozzle-to-work distance	14 mm
Torch angle	Neutral (0°)

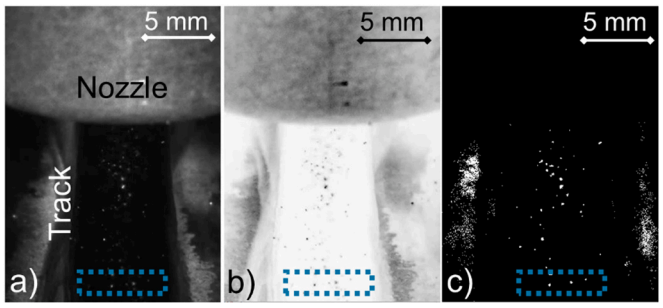

Fig. 3. a) Process image after deposition of a layer which is b) inverted and c) filtered by background subtraction, with the region of interest outlined in blue.

shown in Fig. 12 and 13. The area covered by cavities in Fig. 16 is the average area covered by cavities in one layer.

2.4. Material analysis

For analyzing the pore formation in WAAM, longitudinal cross-sections through the center of the walls were performed. In the cross-sections the porosity was analysed by manually measuring the number and size of pores, with a minimum size of 0.5 mm. The relative number of pores in Fig. 16 is the average number of pores in one layer, counted manually in the cross-section. In addition to the cross-sections, SEM (scanning electron microscope), and EDX (energy dispersive X-ray spectroscopy) scans were carried out. A Scios DualBeam system (Thermo Fisher Scientific, USA) equipped with an EDX spectrometer (EDAX, USA) was used. The microstructure and the elemental distribution of selected elements of the alloy were analysed with SEM and EDX images respectively. In the EDX scans the bright areas represent the presence of the analysed element and different colours are used for differentiation between the elements. A wall and its cross-section with the area in which the SEM/EDX images were taken is shown in Fig. 4.

2.5. Computational Fluid Dynamics simulation

In order to investigate the influence of gas flow on pore formation Computational Fluid Dynamics (CFD) simulations in the Siemens STAR-CCM+ software were carried out to visualise and analyse the inert gas flow on a flat substrate for different gas flow rates. The gas flow simulation was performed in the process zone with a polyhedral mesh as shown in Fig. 5. The basic mesh size is about 1 mm in the coarse areas and about 0.4 mm in the fine areas. In addition, six prism layers were created along the contours of the volume section in order to capture the near-wall effects. In the CFD simulations of different gas flow rates, the axi-symmetric structure of the torch was used to generate the mesh. The gas flow was considered as laminar flow and calculated with the Reynolds-Averaged Navier-Stokes model. The gas flow was modelled as

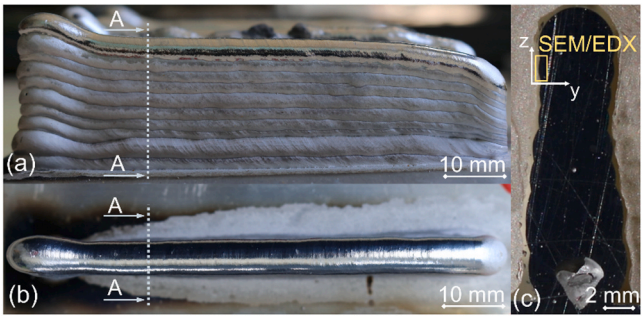

Fig. 4. a) Side view and b) top view of the aluminium wall manufactured by WAAM at a gas flow rate of 10 l/min with its c) cross-section A-A which is embedded in a polymer.

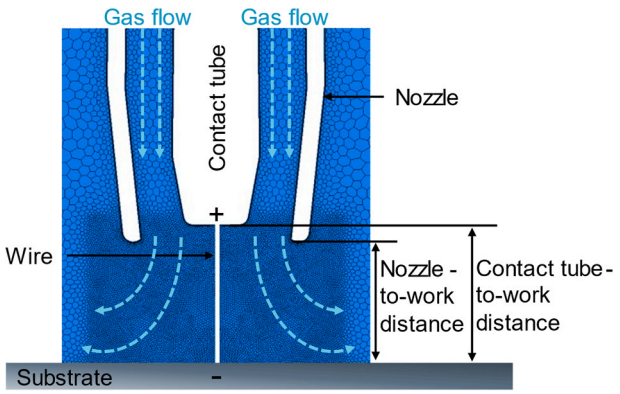

Fig. 5. Mesh of the WAAM torch in the CFD simulation (2D cross section of the 3D simulation domain of the WAAM torch).

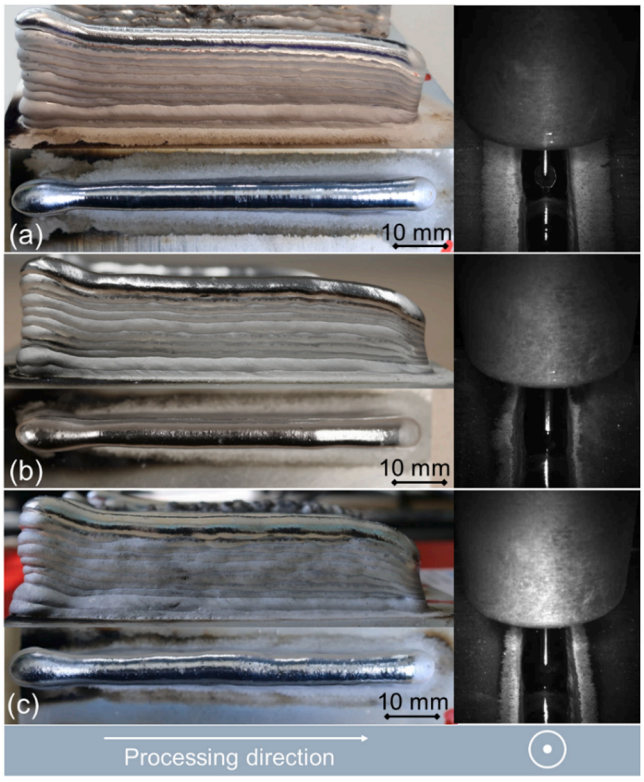

Fig. 6. Resulting walls (side and top view) and corresponding process images during the process in the fifth layer at a gas flow rate of a) 10 l/min, b) 8 l/min, and c) 6 l/min.

an ideal multi-component gas with two different phases; argon and air. A steady state simulation was carried out because the flow conditions in WAAM do not change over time and the robot travel speed was neglected. Isothermal conditions and a segregated flow solver were used in the simulations.

3. Results

3.1. Porosity behaviour for different gas flow rates in WAAM of aluminium

The aluminium walls manufactured at gas flow rates of 10 l/min, 8 l/min, and 6 l/min and their corresponding process images from the process camera are shown in Fig. 6. The geometrical structure of the walls as well as the process images were similar for all gas flow rates and

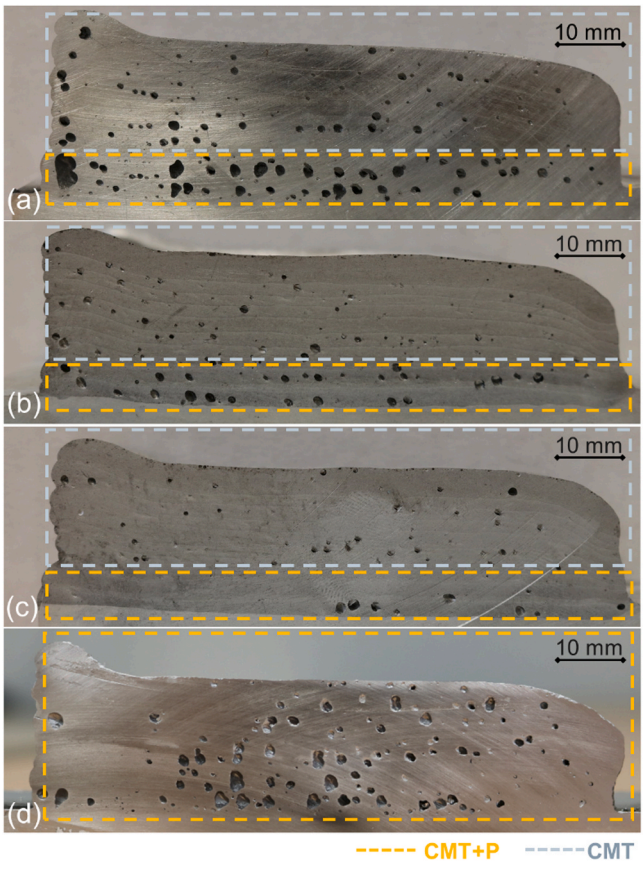

Fig. 7. Longitudinal cross-sections of the walls manufactured at gas flow rates of a) 10 l/min, b) 8 l/min, c) 6 l/min with the first two layer manufactured in CMT+P (marked yellow) and the following eight layer manufactured in CMT (marked grey), and d) the cross-section of a wall manufactured completely by CMT+P at a gas flow rate of 10 l/min.

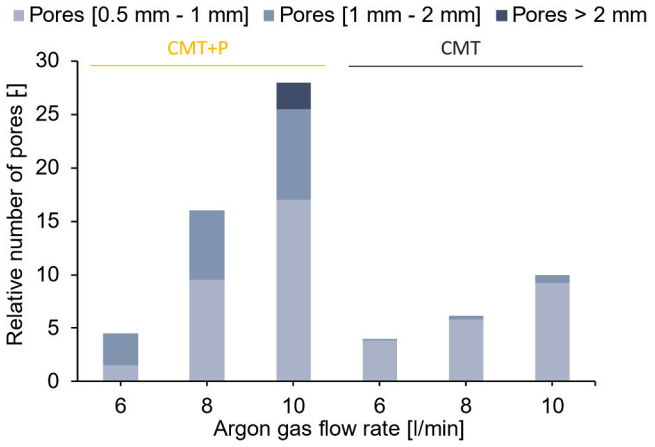

Fig. 8. Relative number of pores per layer in the CMT+P mode and CMT mode for the walls manufactured at different gas flow rates.

all walls had adequate bonding to the substrate.

To obtain details about the porosity, cracks, or delamination effects in the walls, cross-sections were made. In the cross-sections of the walls, shown in Fig. 7, it was observed that the level of porosity increases for an increasing gas flow rate. Furthermore, the pores in the first two layers, which were manufactured with the CMT+P mode, tend to be bigger than the pores in the subsequent layers. The reason for the bigger pores was the pulsed CMT+P mode, which was shown by an additional experiment

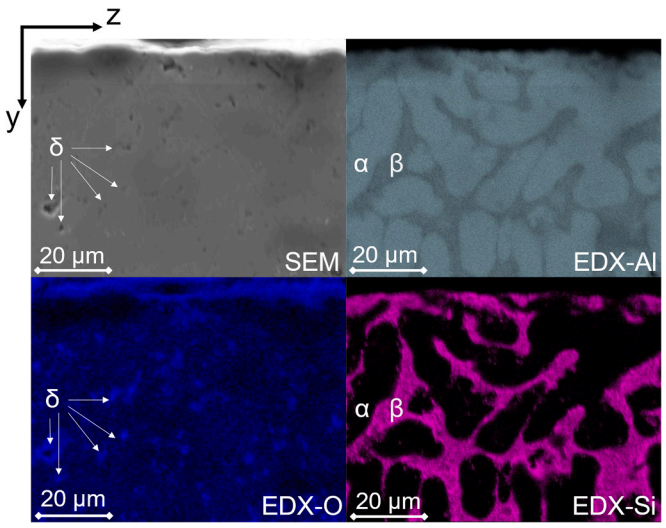

Fig. 9. SEM and EDX scans of aluminium, oxygen, and silicon, analysed in the marked region of Fig. 4. The bright areas indicate that the analysed element is present. They show pure aluminium phases (α), aluminium-silicon composite phases (β), and small pores (δ).

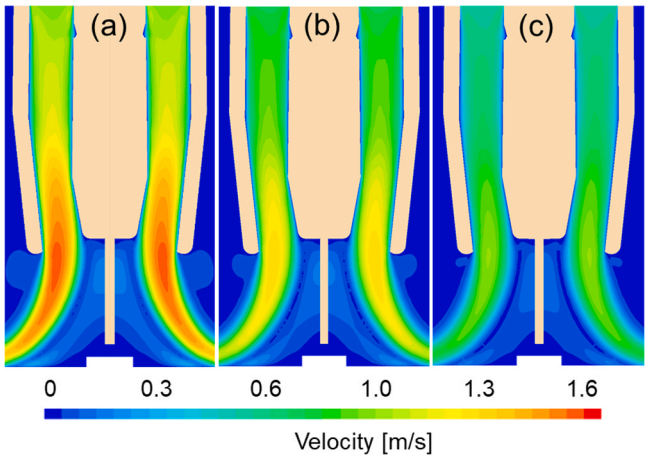

Fig. 10. Gas velocity profiles through the torch for gas flow rates of a) 10 l/min, b) 8 l/min, and c) 6 l/min.

in which a wall was manufactured completely by CMT+P (Fig. 7d). Cracks and delamination defects were not detected. The relative number of pores per layer at different gas flow rates are shown in the graph of Fig. 8. The relative number of pores in the CMT+P mode at 10 l/min is approximately double the value at 8 l/min and more than five times the value at 6 l/min. Pores bigger than 2 mm occurred only at a gas flow rate of 10 l/min. In the CMT mode a similar trend is shown but the relative number of pores is generally smaller. Nevertheless, the number of pores in the wall produced at a gas flow rate of 10 l/min is twice as high as at 6 l/min.

The wall manufactured at a gas flow rate of 10 l/min was analysed by SEM and EDX scans. The wall and its cross-section, with its area in which the SEM/EDX images were performed, are shown in Fig. 4. The SEM and EDX images, in which pure aluminium phases (α), aluminium-silicon composite phases (β), and small pores (δ) were found, are shown in Fig. 9. The EDX scans for aluminium (EDX-Al) and silicon (EDX-Si) show that the walls manufactured by WAAM consist of pure aluminium phases (α) and aluminium-silicon composite phases (β). No cracks or major defects were detected in the SEM image. However, small pores (δ) were detected in the SEM image and these pores were also visible in the EDX image for oxygen. Within the area of the pores the analysed oxygen level

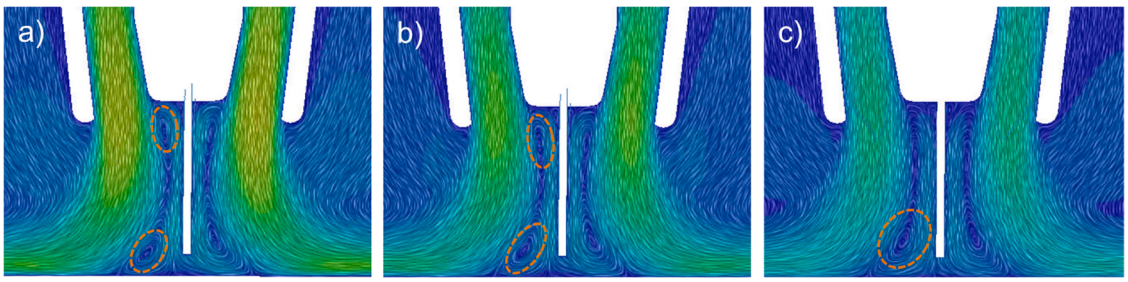

Fig. 11. Stream lines of the argon gas flow for gas flow rates of a) 10 l/min, b) 8 l/min, and c) 6 l/min with recirculation effects (marked orange).

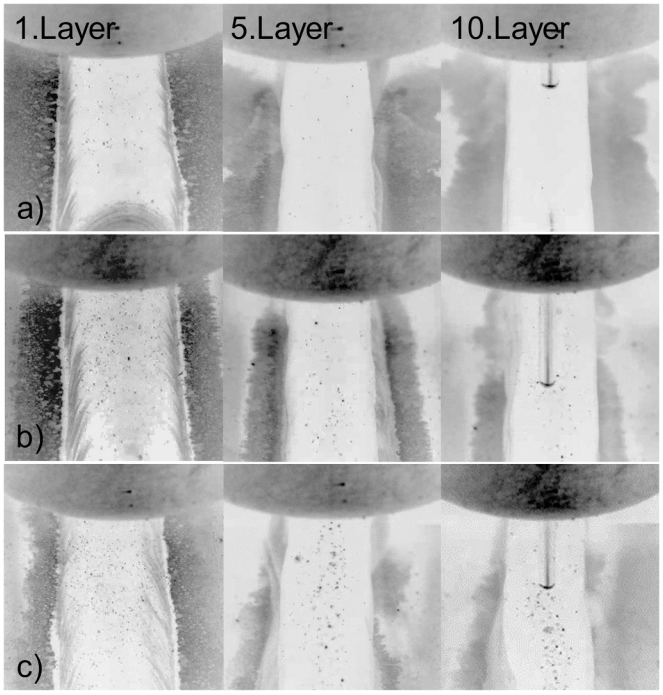

Fig. 12. Inverted process images recorded with the coaxial process camera after the first layer, the fifth layer, and the tenth layer of the walls manufactured at a gas flow rate of a) 10 l/min, b) 8 l/min, and c) 6 l/min, in which the cavities (black dots) on the layer are visible.

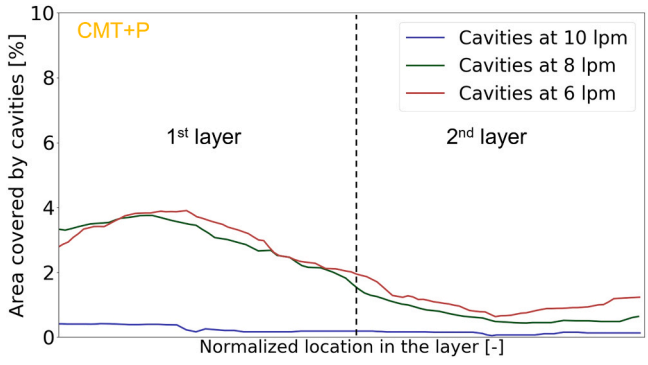

Fig. 13. Detection of the cavities in the solidified layers produced by CMT+P.

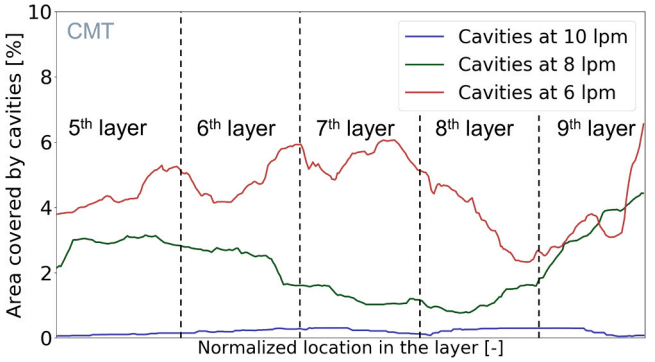

Fig. 14. Detection of the cavities in the solidified layers produced by CMT.

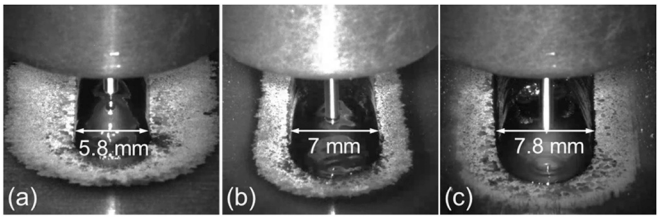

Fig. 15. Melt pool width in the first layer of the walls manufactured at a gas flow rate of 10 l/min (a), 8 l/min (b), and 6 l/min (c).

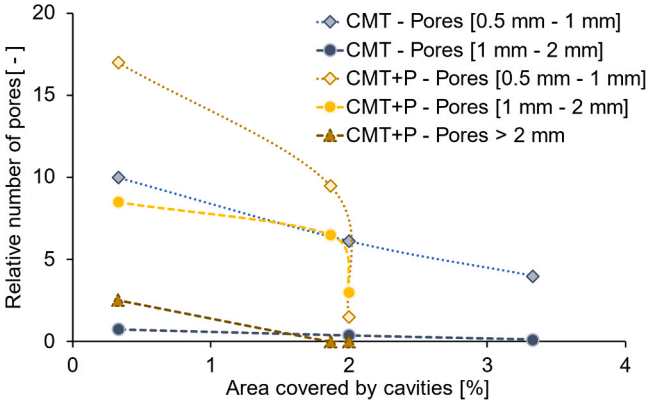

Fig. 16. Correlation of the relative number of pores, counted manually in the cross-section, with the relative covered area by cavities in one layer.

and thus the aluminium oxide content is substantially higher than in the total area analysed.

The different gas flow rates of 6 l/min, 8 l/min, and 10 l/min, were simulated in CFD to obtain a better understanding about the influence of the gas flow on the process and the part manufactured. The velocity profiles at gas flow rates of 6 l/min, 8 l/min, and 10 l/min were simulated and are shown in Fig. 10. The simulations revealed that the velocity profile and thus the dynamic gas pressure at a gas flow rate of 8 l/min is about 25% lower and at a gas flow rate of 6 l/min even 40% lower as at a gas flow rate of 10 l/min. This indicates that higher gas flow rates result in a higher level of forced convective cooling of the material

deposited. Furthermore, the stream lines of the different gas flow rates, shown in Fig. 11, revealed recirculation effects, which increased at higher gas flow rates. These recirculation effects were induced by the relative movement of the gas flow and the wire to each other. These recirculation effects decreased with a lower gas flow rate.

3.2. Process monitoring

The top view of the walls (Fig. 6) showed that the surface roughness increases for lower gas flow rates. At a gas flow rate of 10 l/min the surface on top of the wall was smooth, but at a gas flow rate of 6 l/min the surface was rougher, due to the presence of cavities and spatter. During WAAM no major differences were observed in the process images because the melt pool was still liquid. However, on the way back to the starting position, the previously deposited layer was already solidified, and cavities were visible on its surface. In order to increase the visibility of these cavities, the process images were inverted as shown in Fig. 11. It was observed that, for all the layers, the number of cavities (black dots) increased for a lower gas flow rate. Also, the number of cavities in the first layer, which was processed by CMT+P, was higher due to the higher number of pores which occur in that mode.

To investigate this phenomenon further, a computer vision algorithm, following the procedure shown in Fig. 3 was developed. The algorithm analyses the percentage area covered by cavities on the surface over time. The percentage share of the region of interest covered by cavities in the different layers is shown for the process modes CMT+P in Fig. 12 and CMT in Fig. 13. In the first two layers of the walls manufactured at a gas flow rate of 6 l/min and 8 l/min the graphs show almost the same values. Both walls show a significantly bigger area covered by cavities than the wall manufactured at a gas flow rate of 10 l/min, which correlates with the lower porosity at 6 l/min and 8 l/min compared to 10 l/min. For the wall manufactured at 10 l/min almost no cavities were detected because less pores were escaping from the melt pool during solidification.

In the CMT mode the graphs from layers three to nine were plotted. The diagrams show that the average number of cavities is generally higher than for CMT+P in all layers and that higher gas flows result in fewer 'bursting bubble' cavities. Similarly, to the CMT+P case, there is a clear inverse correlation between the number of cavities and the retained porosity.

4. Discussion

4.1. Porosity induced by ambient gas

The high proportion of large pores in the walls indicates that process related pores occurred due to the incorporation of air (oxygen and nitrogen) which cannot escape from the melt pool [18]. This suggestion is supported by the EDX images shown in Fig. 9, in which it is clear that the content of aluminium oxide is substantially elevated in the areas around the pores. This observation indicates that the pores were in contact with oxygen, which reacted with aluminium to form aluminium oxide. The oxygen most likely came from the ambient air, which entered the process zone because of recirculation effects. The higher gas velocities (Fig. 10) and the higher dynamic gas pressure at higher gas flow rates lead to more process pores because of increased recirculation effects in the gas flow (Fig. 11). Further reasons for oxygen entering the process zone could be the dissociation of aluminium oxide from the wire and from the substrate. The arc, reaching a temperature of up to 10,000 K, splits the aluminium oxide into aluminium and oxygen. The resulting oxygen could easily enter the melt pool since the aluminium is melted by the arc at the same moment.

4.2. Shielding gas influence on the melt pool

It is important to note that a higher gas flow rate increases the convective cooling of the melt pool. If the melt pool is cooled more effectively in this way it will have a higher viscosity and a smaller surface area, both of which inhibit the ejection of pores from the melt. To investigate this further, the melt pool width was measured, as shown in Fig. 14. From these measurements it was noted that the melt pool width increased by about 20% with a reduction of the gas flow rate from 10 l/min to 8 l/min. Reducing the gas flow rate from 8 l/min to 6 l/min increased the melt pool width by a further 11%. This observation supports the theory of higher forced convection with higher gas flow rates and is consistent with the observations of higher porosity with higher gas flow rates.

4.3. Mechanism of gas bubble escape

As noted above, in addition to the porosity, cavities were found on the top of the walls that were produced. These cavities are probably created at the moment that gas pores escape from the melt pool, leaving an open pore on the surface of the layer. The number of cavities increased at a lower gas flow rate and therefore, a correlation of these cavities with the pore content was considered. In the process images of each layer, for instance in layer one, five, and ten (Fig. 11), cavities were found. It was observed that as the gas flow rate decreased, the number of cavities increased. In addition, the pore content decreases with decreasing gas flow rate (Fig. 7), which indicates that a higher number of cavities correlates with lower porosity within the part. This was examined further by correlating the relative number of pores with the area covered by cavities, as shown in Fig. 15. In the figure the results for small (0.5–1 mm), medium (1–2 mm) and big pores (>2 mm) for CMT and CMT+P are presented. The correlation between the relative number of pores and the area covered by cavities is linear descending for CMT and non-linear descending for CMT+P in the chosen range of parameters. The graphs also show a similar trend for all pore sizes in these process modes. In CMT+P the energy input is higher and thus the melt pool remains liquid for a longer period. Therefore, the number of gas inclusions which escape before solidification is higher in the CMT+P mode which could explain the limit of detectable cavities at 2%.

The creation of cavities by gas inclusions escaping from the melt pool is illustrated in Fig. 16. The most likely reason for higher numbers of pores escaping from the aluminium melt pool is reduced melt cooling related to a lower shielding gas flow rate. The main factors of heat dissipation from the melt pool are conduction (Q_{cd}) and convection effects (Q_{cv}). The convection effects are mainly related to the shielding gas, as shown in Fig. 16. Since a lower gas flow rate leads to reduced convection effects, the melt pool, and especially the surface of the melt pool, remains liquid for a longer period. Thus, pores can escape for a longer period as well. (Fig. 17).

In summary, a higher number of cavities on the surface correlates with a smaller number of pores in the layer. In general, the proportion of cavities on the solidified surface therefore suggests the relative number of pores in an aluminium part manufactured by WAAM. It is worth bearing in mind that the cavities and spatter, caused by escaping gas pores, could act like small notches on the surface of the part, reducing the mechanical properties by stress raising effects. However, in the body of the wall, both in the cross-sections and in the image data of the process camera, it was found that the area covered by cavities and spatter is remelted by any subsequent layer and any internal 'notches' are thus neutralised.

5. Conclusions

In the present work, pore formation in Wire Arc Additive Manufacturing of AW4043/AlSi5(wt%) was investigated. Process imaging was used to capture image data and to monitor pore formation or pore escape during WAAM. The observations were supported by CFD simulations. The following conclusions could be drawn:

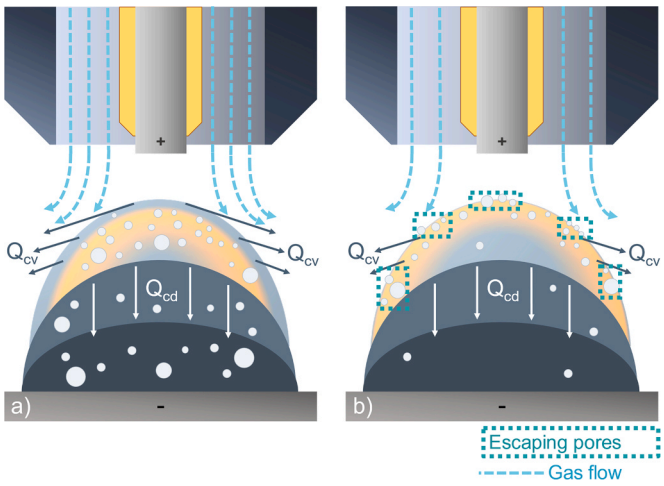

Fig. 17. Sketch of the cross-section showing the influence of the gas flow rate on solidification and pore behaviour of the layer for a) higher gas flow rates and b) lower gas flow rates.

- Process-related pores were found in the parts manufactured by WAAM. They were most likely caused by the shielding gas mixing with the ambient air because the pores showed a substantially higher content of aluminium oxide in these areas.
- Higher shielding gas flow rates with higher velocities and higher dynamic gas pressure lead to more process related pores, probably because of increased turbulent mixing.
- Further sources of oxygen could be the aluminium oxide of the wire and the substrate, which dissociates in the arc-based process and could enter the melt pool.
- The higher number of pores in aluminium parts is related to the shielding gas flow rate, because at a higher gas flow rate, the melt pool solidifies faster as a result of increased convective cooling, thus preventing the process-related gas inclusions from escaping.
- The number of cavities on the surface of each deposited layer is inversely related to the relative number of pores in an aluminium part manufactured by WAAM. A higher number of cavities on the surface correlates with a lower number of pores in the part because cavities are gas inclusions that have escaped from the melt pool. The relative number of pores decreases linearly in the CMT mode and non-linearly in the CMT+P mode as the relative area covered by cavities increases.
- Some aluminium alloys such as AlSi5 are likely to suffer from process related pores. That being the case, a monitoring approach of the percentage area covered by cavities is a suitable method to monitor pore formation in the part. Based on this, an in-situ monitoring with a closed loop control system could be established.

CRediT authorship contribution statement

Tobias Hauser: Conceptualization, Methodology, Software, Validation, Investigation, Writing - original draft, Writing - review & editing, Visualization. **Raven Thomas Reisch:** Methodology, Writing - review & editing. **Philipp Peter Breese:** Formal analysis, Investigation, Writing - review & editing. **Benjamin Samuel Lutz:** Software, Writing - review & editing. **Matteo Pantano:** Software, Writing - review & editing. **Yogesh Nalam:** Formal analysis. **Katharina Bela:** Investigation, Writing - review & editing. **Tobias Kamps:** Project administration, Funding acquisition, Supervision. **Jörg Volpp:** Project administration, Funding acquisition, Writing - review & editing, Supervision. **Alexander F.H. Kaplan:** Writing - review & editing, Supervision.

Declaration of Competing Interest

The authors declare that they have no known competing financial interests or personal relationships that could have appeared to influence the work reported in this paper.

Acknowledgement

The authors gratefully acknowledge funding from EIT RawMaterials (Initiated and funded by the European Institute of Innovation and Technology) for the project SAMOA - Sustainable Aluminium additive Manufacturing for high performance Applications, no. 18079. Furthermore, the authors acknowledge the technical and formal advice by Dr. John Powell (Visiting Professor at Luleå University in Sweden and Nottingham University in UK).

References

[1] K.S. Derekar, A review of wire arc additive manufacturing and advances in wire arc additive manufacturing of aluminium, Mater. Sci. Technol. 34 (2018) 895–916, https://doi.org/10.1080/02670836.2018.1455012.
[2] L.E.J. Thomas-Seale, J.C. Kirkman-Brown, M.M. Attallah, D.M. Espino, D.E. T. Shepherd, The barriers to the progression of additive manufacture: perspectives from UK industry, Int. J. Prod. Econ. 198 (2018) 104–118, https://doi.org/10.1016/j.ijpe.2018.02.003.
[3] T. DebRoy, H.L. Wei, J.S. Zuback, T. Mukherjee, J.W. Elmer, J.O. Milewski, A. M. Beese, A. Wilson-Heid, A. De, W. Zhang, Additive manufacturing of metallic components – process, structure and properties, Prog. Mater. Sci. 92 (2018) 112–224, https://doi.org/10.1016/j.pmatsci.2017.10.001.
[4] S. Zielińska, K. Musioł, K. Dzierżęga, S. Pellerin, F. Valensi, C. de Izarra, F. Briand, Investigations of GMAW plasma by optical emission spectroscopy, Plasma Sources Sci. Technol. 16 (2007) 832–838, https://doi.org/10.1088/0963-0252/16/4/019.
[5] T. Hauser, A.D. Silva, R.T. Reisch, J. Volpp, T. Kamps, A.F.H. Kaplan, Fluctuation effects in Wire Arc Additive Manufacturing of aluminium analysed by high-speed imaging, J. Manuf. Process. 56 (2020) 1088–1098, https://doi.org/10.1016/j.jmapro.2020.05.030.
[6] P. Kazanas, P. Deherkar, P. Almeida, H. Lockett, S. Williams, Fabrication of geometrical features using wire and arc additive manufacture, Proc. Inst. Mech. Eng. Part B J. Eng. Manuf. 226 (2012) 1042–1051, https://doi.org/10.1177/0954405412437126.
[7] A.G. Ortega, L. Corona Galvan, M. Salem, K. Moussaoui, S. Segonds, S. Rouquette, F. Deschaux-Beaume, Characterisation of 4043 aluminium alloy deposits obtained by wire and arc additive manufacturing using a Cold Metal Transfer process, Sci. Technol. Weld. Join. 24 (2019) 538–547, https://doi.org/10.1080/13621718.2018.1564986.
[8] T.A. Rodrigues, V. Duarte, R.M. Miranda, T.G. Santos, J.P. Oliveira, Current status and perspectives on wire and Arc Additive Manufacturing (WAAM), Materials 12 (2019) 1121, https://doi.org/10.3390/ma12071121.
[9] C. Zhou, H. Wang, T.A. Perry, J.G. Schroth, On the analysis of metal droplets during cold metal transfer, Procedia Manuf. 10 (2017) 694–707, https://doi.org/10.1016/j.promfg.2017.07.024.
[10] S. Selvi, A. Vishvaksenan, E. Rajasekar, Cold metal transfer (CMT) technology - an overview, Def. Technol. 14 (2018) 28–44, https://doi.org/10.1016/j.dt.2017.08.002.
[11] F. Wang, S. Williams, P. Colegrove, A.A. Antonysamy, Microstructure and mechanical properties of wire and arc additive manufactured Ti-6Al-4V, Met. Mat. Trans. A 44 (2013) 968–977, https://doi.org/10.1007/s11661-012-1444-6.
[12] X. Fang, L. Zhang, G. Chen, X. Dang, K. Huang, L. Wang, B. Lu, Correlations between microstructure characteristics and mechanical properties in 5183 aluminium alloy fabricated by Wire-arc Additive Manufacturing with different arc modes, Materials (2018), https://doi.org/10.3390/ma11112075.
[13] H. Geng, J. Li, J. Xiong, X. Lin, F. Zhang, Geometric limitation and tensile properties of wire and arc additive manufacturing 5A06 aluminum alloy parts, J. Mater. Eng. Perform. 26 (2017) 621–629, https://doi.org/10.1007/s11665-016-2480-y.
[14] R. Kaibyshev, F. Musin, D.R. Lesuer, T.G. Nieh, Superplastic behavior of an Al–Mg alloy at elevated temperatures, Mater. Sci. Eng.: A 342 (2003) 169–177, https://doi.org/10.1016/S0921-5093(02)00276-9.
[15] U. Dilthey, Schweißtechnische Fertigungsverfahren 2: Verhalten der Werkstoffe beim Schweißen, Dritte bearbeitete Auflage, Springer-Verlag Berlin Heidelberg, Berlin, Heidelberg, 2005.
[16] Le Zhou, H. Hyer, S. Park, H. Pan, Y. Bai, K.P. Rice, Y. Sohn, Microstructure and mechanical properties of Zr-modified aluminum alloy 5083 manufactured by laser powder bed fusion, Addit. Manuf. 28 (2019) 485–496, https://doi.org/10.1016/j.addma.2019.05.027.
[17] M. Köhler, S. Fiebig, J. Hensel, K. Dilger, Wire and Arc Additive Manufacturing of aluminum components, Metals 9 (2019) 608, https://doi.org/10.3390/met9050608.
[18] Aluminium-Zentrale, Aluminium-Taschenbuch, Aluminium-Verlag, Duesseldorf, 1988.

[19] J. Gu, J. Ding, S.W. Williams, H. Gu, P. Ma, Y. Zhai, The effect of inter-layer cold working and post-deposition heat treatment on porosity in additively manufactured aluminum alloys, J. Mater. Process. Technol. 230 (2016) 26–34, https://doi.org/10.1016/j.jmatprotec.2015.11.006.

[20] K. Derekar, J. Lawrence, G. Melton, A. Addison, X. Zhang, L. Xu, Influence of interpass temperature on Wire Arc Additive Manufacturing (WAAM) of aluminium alloy components, MATEC Web Conf. 269 (2019) 05001, https://doi.org/10.1051/matecconf/201926905001.

[21] J. Bai, H.L. Ding, J.L. Gu, X.S. Wang, H. Qiu, Porosity evolution in additively manufactured aluminium alloy during high temperature exposure, IOP Conf. Ser. Mater. Sci. Eng. 167 (2017), 012045, https://doi.org/10.1088/1757-899X/167/1/012045.

[22] C. Chen, X. Wei, Y. Zhao, K. Yan, Z. Jia, Y. He, Effects of helium gas flow rate on arc shape, molten pool behavior and penetration in aluminum alloy DCEN TIG welding, J. Mater. Process. Technol. 255 (2018) 696–702, https://doi.org/10.1016/j.jmatprotec.2017.12.029.

[23] B.Y. Kang, Y.K.D.V. Prasad, M.J. Kang, H.J. Kim, I.S. Kim, Characteristics of alternate supply of shielding gases in aluminum GMA welding, J. Mater. Process. Technol. 209 (2009) 4716–4721, https://doi.org/10.1016/j.jmatprotec.2008.11.036.

[24] D. Wang, J. Lu, S. Tang, L. Yu, H. Fan, L. Ji, C. Liu, Reducing porosity and refining grains for arc additive manufacturing aluminum alloy by adjusting arc pulse frequency and current, Materials 11 (2018), https://doi.org/10.3390/ma11081344.

[25] B. Cong, J. Ding, S. Williams, Effect of arc mode in cold metal transfer process on porosity of additively manufactured Al-6.3%Cu alloy, Int J. Adv. Manuf. Technol. 76 (2015) 1593–1606, https://doi.org/10.1007/s00170-014-6346-x.

[26] Y. Javadi, C.N. MacLeod, S.G. Pierce, A. Gachagan, D. Lines, C. Mineo, J. Ding, S. Williams, M. Vasilev, E. Mohseni, R. Su, Ultrasonic phased array inspection of a Wire + Arc Additive Manufactured (WAAM) sample with intentionally embedded defects, Addit. Manuf. 29 (2019), 100806, https://doi.org/10.1016/j.addma.2019.100806.

[27] J.B. Bento, A. Lopez, I. Pires, L. Quintino, T.G. Santos, Non-destructive testing for Wire + Arc Additive Manufacturing of aluminium parts, Addit. Manuf. 29 (2019), 100782, https://doi.org/10.1016/j.addma.2019.100782.

[28] Y. Ma, Z. Hu, Y. Tang, S. Ma, Y. Chu, X. Li, W. Luo, L. Guo, X. Zeng, Y. Lu, Laser opto-ultrasonic dual detection for simultaneous compositional, structural, and stress analyses for Wire + Arc Additive Manufacturing, Addit. Manuf. 31 (2020), 100956, https://doi.org/10.1016/j.addma.2019.100956.

[29] A. Lopez, R. Bacelar, I. Pires, T.G. Santos, J.P. Sousa, L. Quintino, Non-destructive testing application of radiography and ultrasound for Wire and Arc Additive Manufacturing, Addit. Manuf. 21 (2018) 298–306, https://doi.org/10.1016/j.addma.2018.03.020.

[30] Q. Zhan, Y. Liang, J. Ding, S. Williams, A wire deflection detection method based on image processing in wire + arc additive manufacturing, Int J. Adv. Manuf. Technol. 89 (2017) 755–763, https://doi.org/10.1007/s00170-016-9106-2.

[31] B. Zhang, S. Liu, Y.C. Shin, In-process monitoring of porosity during laser additive manufacturing process, Addit. Manuf. 28 (2019) 497–505, https://doi.org/10.1016/j.addma.2019.05.030.

[32] R. Reisch, T. Hauser, T. Kamps, A. Knoll, Robot based Wire Arc Additive Manufacturing system with context-sensitive multivariate monitoring framework: 30th international conference on flexible automation and intelligent manufacturing, Procedia Manuf. 51 (2020) 732–739, https://doi.org/10.1016/j.promfg.2020.10.103.

[33] Q. Miao, D. Wu, D. Chai, Y. Zhan, G. Bi, F. Niu, G. Ma, Comparative study of microstructure evaluation and mechanical properties of 4043 aluminum alloy fabricated by wire-based additive manufacturing, Mater. Des. 186 (2020), 108205, https://doi.org/10.1016/j.matdes.2019.108205.